ARCHIVIO ISTITUZIONALE
DELLA RICERCA

Alma Mater Studiorum Università di Bologna
Archivio istituzionale della ricerca

A357 aluminium alloy produced by LPBF: Tribological behaviour in dry sliding conditions

This is the final peer-reviewed author's accepted manuscript (postprint) of the following publication:

Published Version:
Lorenzetti, L., Tonelli, L., Ceschini, L., Liverani, E., Martini, C. (2022). A357 aluminium alloy produced by LPBF: Tribological behaviour in dry sliding conditions. WEAR, 510-511, 1-13 [10.1016/j.wear.2022.204488].

Availability:
This version is available at: https://hdl.handle.net/11585/897397 since: 2023-02-28

Published:

DOI: http://doi.org/10.1016/j.wear.2022.204488

Terms of use:

Some rights reserved. The terms and conditions for the reuse of this version of the manuscript are specified in the publishing policy. For all terms of use and more information see the publisher's website.

This item was downloaded from IRIS Università di Bologna (https://cris.unibo.it/).
When citing, please refer to the published version.

(Article begins on next page)

28 March 2025

This is the final peer-reviewed accepted manuscript of:

Luca Lorenzetti, Lavinia Tonelli, Lorella Ceschini, Erica Liverani, Carla Martini, *A357 Aluminium alloy produced by LPBF: tribological behaviour in dry sliding conditions*, Wear (2022), 510-511, pp. 204488.

The final published version is available online at:

https://doi.org/10.1016/j.wear.2022.204488

Rights / License: CC-BY-NC-ND 4.0 license (http://creativecommons.org/licenses/by-nc-nd/4.0/)

The terms and conditions for the reuse of this version of the manuscript are specified in the publishing policy. For all terms of use and more information see the publisher's website.

*This item was downloaded from IRIS Università di Bologna (*https://cris.unibo.it/*)*

When citing, please refer to the published version.

A357 Aluminium alloy produced by LPBF: tribological behaviour in dry sliding conditions

L. Lorenzetti[a*], L. Tonelli[a], L. Ceschini[a], E. Liverani[b], C. Martini[a]

[a] *Department of Industrial Engineering (DIN), Alma Mater Studiorum, University of Bologna, Viale Risorgimento 4, 40136 Bologna, Italia*
[b] *Interdepartmental Center for Industrial Research on Advanced Mechanics and Materials (CIRI-MAM), Alma Mater Studiorum, University of Bologna, Italia.*

*Corresponding author: Luca Lorenzetti, *Department of Industrial Engineering, Alma Mater Studiorum, University of Bologna, Viale Risorgimento 4, 40136, Bologna, Italy* (luca.lorenzetti5@unibo.it)

Abstract

Laser Powder Bed Fusion (LPBF) is increasingly used in packaging, automotive and aerospace sectors for manufacturing Al alloy components where fatigue and wear damage can readily occur. Therefore, this work aims to assess the tribological behaviour of A357 alloy (AlSi7Mg0.6) produced by LPBF as a function of both printing parameters and heat treatment conditions, applying a novel T6 based on rapid solution followed by artificial aging, which improves the strength-ductility balance. Dry sliding tests (block-on-ring) were performed using A357 samples as stationary blocks against rotating quenched and tempered AISI 52100 (100Cr6) steel. LPBF samples were compared with A357 obtained by sand casting, subjected to Hot Isostatic Pressing (HIP) and conventional T6 heat treatment. Microstructural refinement induced by LPBF carried out in optimized conditions, even without post-processing treatments, reduced the wear rate in comparison to conventional sand-cast, HIP-ped and T6 heat-treated A357, while maintaining comparable coefficient of friction. The rapid solution T6 did not worsen the tribological behaviour of as-built LPBF A357 components, even though it induced a slight hardness decrease.

Keywords: Sliding wear, Non-ferrous metals, Other manufacturing process, Electron microscopy, Surface topography, Wear testing

1. Introduction

The most widespread powder bed based Additive Manufacturing technology (AM) known as Laser Powder Bed Fusion (LPBF) is increasingly used to produce lightweight metallic components for engineering applications, especially in automotive, aerospace and aeronautics. Based on layer-by-layer selective fusion of very fine metal powders, LPBF process allows a freedom of design impossible to achieve by conventional technologies, with a remarkable simplification of the manufacturing cycle and significant raw materials saving, also thanks to the possibility of recycling pre-utilized powders [1].

In this context, AlSiMg alloys are extensively studied, thanks to their high corrosion resistance, low thermal expansion, good castability and high strength-to-weight ratio, generally improved by aging treatment [2]. These features make conventional casting AlSiMg alloys suitable for applications such as pump parts, valve bodies, automotive transmission cases and cylinder blocks [3]. A357 (AlSi7Mg0.6) in particular is used for automotive and aerospace components which require heat-treatable castings, high strength and fairly good ductility [4]. The interest towards these alloys is growing also in the packaging industry [5], where the strength-toughness combination afforded by this alloy allows component lightweighting and hence higher process efficiency as well as energy consumption reduction. Sliding contacts are very frequent in this sector (e.g. guide plates vs. pins

and/or shafts in tablet pressing devices): the identification of materials which satisfy also the wear resistance requirements is one of the main tribological challenges faced by this industry. Based on the interest for this kind of applications, where non-conformal line contacts are very frequent, in this work sliding tests were carried out in the block-on-ring contact geometry.

The Al-Si-Mg alloys microstructure obtained by LPBF differs substantially from those produced with conventional casting technologies. The LPBF high thermal gradient and cooling rates allows the formation of a solid supersaturated solution, characterized by an extremely fine microstructure, which leads to high strength already in the as-built condition [6]. However, while there are many reports on the mechanical, static and fatigue behaviour of Al alloys produced by LPBF, their dry sliding behaviour is still under investigation and published data are substantially limited to AlSi12Mg and AlSi10Mg alloys [7–13]. Considering the as-built condition, both LPBF AlSi12 [7] and AlSi10Mg [8] showed lower wear rates when compared with the corresponding casting alloy, when dry sliding against hard-faced stainless steel and EN31 steel (equivalent to 100Cr6), respectively. Similar results were obtained also by Wu *et al.* [9], demonstrating that as-built LPBF AlSi10Mg displayed improved wear resistance in comparison to the same as-cast alloy when sliding against GCr15 bearing steel (equivalent to 100Cr6), in unlubricated condition. The Authors ascribed these findings to the combination of microstructural refinement and higher surface hardness derived from the high cooling rate of LPBF [7–9]. Interestingly, LPBF AlSi10Mg retained better tribological properties even when tested at elevated temperature (200 °C), where the formation of a protective oxide glaze layer lead to a reduction in direct metal-to-metal contact [8]. Also scanning strategy and process parameters usually affect both density and microstructural fineness, in turn affecting the dry sliding behaviour of Al-Si alloys vs G-Cr15 bearing steel. For instance, Kang *et al.* [10] claimed that LPBF AlSi12 had a lower wear rate than hot-extruded Al-Si-Cu, depending on the power of the laser source. Liu et al. [11] observed an improvement of the tribological properties of AlSi12 using a chessboard-type scanning pattern, whilst Wu *et al.* [9] reported lower wear rates using a higher energy density (i.e. $E = 83.33\ J / mm^3$ vs $E = 42.03\ J / mm^3$). For all the previously mentioned works, the main wear mechanisms of LPBF Al-Si alloys were a combination of abrasive and tribo-oxidative phenomena, with adhesion increasing as contact conditions became increasingly severe [7,11–13].

Therefore, several papers demonstrated the superior tribological behaviour of as-built LPBF Al-Si alloys in comparison to conventional casting Al-Si products. However, for specific applications requiring a trade-off between tensile strength and ductility, the possibility to use heat treatments cannot be overlooked [14]. To this regard, several Authors found that post-print annealing treatments produced an increase in wear rate under unlubricated conditions at room temperature: Prashant *et al.* [7] claimed that microstructural coarsening induced by annealing (carried out in the range from 473 and 723 K for 6 h under Ar atmosphere) led to an increase in the wear rate of LPBF AlSi12 when dry sliding against hard-faced stainless steel, more significant with increasing annealing temperature. Likewise, Wei *et al.* [15] stated that the wear resistance of AlSi10Mg, dry sliding against Si_3N_4, decreased with increasing the solution treatment temperature. The effect of T6 heat treatment (including solution treatment, quenching and artificial aging) on the mechanical and wear behaviour of LPBF Al-Si-Mg alloys was investigated by several Authors [8,16–19]. When looking at the influence of T6 on the wear properties of LPBF Al-Si-Mg alloys in dry sliding conditions, experimental studies led to conflicting results: while Tonolini *et al.* [16] reported that, for LPBF AlSi10Mg, the T6-treated alloys showed lower wear resistance against 100Cr6 than in the as-built condition, Park *et al.* [17] stated that T6 improved the wear resistance of LPBF AlSi10Mg alloy against 100Cr6. In the former case, the worst wear behaviour was ascribed to the hardness decrease and significant porosity evolution, while in the latter T6 led to the precipitation of fine Si phases strongly bonded with the Al-rich matrix, providing higher load-bearing capacity and therefore improved wear resistance. Other Authors [20] instead claimed that T6 did not significantly affect the wear rate of LPBF AlSi10Mg alloy against AISI 440C martensitic stainless steel. They concluded

that applying conventional T6 to LPBF AlSi10Mg alloy is generally not necessary to improve its wear behaviour. These conflicting findings probably derived from the combination of both different testing conditions and heat treatment procedures, besides different defect content in the as-built alloy. Nevertheless, since LPBF generates a completely different microstructure in comparison to conventional manufacturing processes, redesigning heat treatment procedures (i.e., with a reduced solution treatment time) is necessary for improving mechanical and tribological properties of the LPBF components. Therefore, investigating new heat treatment methodologies, tailored on the basis of both initial and final microstructure of LPBF-manufactured components is a key issue. To this regard, a novel T6 heat treatment was developed [18], providing promising results when applied to LPBF A357. Characterized by a shorter solution treatment time (i.e. 10 minutes) at 540°C, the novel T6 allowed to reduce anisotropy and promoted a complete residual stress relieving. It enabled to attain higher hardness values thanks to a composite-like microstructure with finer and more dispersed Si particles in comparison to conventional A357 and AlSi10Mg alloys obtained by sand casting [18,21]. To the best of our knowledge, the effect of this novel T6 treatment on the tribological behaviour of LPBF A357 (for which only a limited number of studies, not focusing on the tribological behaviour [22–27], is available) has not been investigated yet.

Based on the above, dry sliding tests were performed on A357 alloy samples produced by LPBF, starting from the same powders but using two sets of process parameters aimed at the improvement of productivity (P) or microstructure (M). LPBF A357 alloy was investigated firstly in the as-built condition and then subjected to the above mentioned novel T6, to evaluate its effect on microstructure evolution and wear resistance. The A357 alloy obtained by sand casting, subjected to Hot Isostatic Pressing (HIP) and conventional T6 was used as benchmark. In the present work, the choice of tribological testing conditions was guided by the increasing interest for the use of aluminium alloys in the packaging industry. In this field, sliding contacts between steel and aluminium alloys are rather frequent, therefore dry sliding tests were carried out using AISI 52100 (100Cr6) bearing steel as the countermaterial.

2. Materials and methods

2.1 A357 LPBF samples production

A357 small bars (5 x 5 x 70 mm^3) were produced by LPBF, starting from a gas atomized powder supplied by LPW Technology Ltd (currently Carpenter Additive, Carpenter Technology Corporation, USA), with the following composition (wt. %): Al 92.1, Si 6.97, Mg 0.55, Fe 0.06, Ti 0.13, Zn 0.08, others 0.11. Prior to the LPBF process, powder was dried at 60 °C for 3 hours to remove humidity [28].

LPBF samples were produced using a MYSINT100 RM machine, produced by SISMA, equipped with a 200 W laser source with a spot diameter of 55 µm. The melting process was conducted in an N_2 atmosphere with a residual oxygen content of 0.1 vol.%. We used N_2 instead of Ar gas based on previous studies that identified the conditions for optimal densification of A357 under N_2 atmosphere [28]. N_2 proved to be as effective as Ar, once inlet flow and gas pressure were optimised, but it was more cost-effective, therefore it was selected for this process.

Samples were manufactured in a single batch on a cold (no pre-heated) aluminium platform, with a vertical building direction, correspondent to the longitudinal (Z) axis of the bars and using conical supports. The main process parameters adopted during the LPBF processes are summarized in Table 1. In particular, based on process parameters, samples were divided in two series: (i) printing in conditions of maximum productivity (P series, with high productivity $Prod_{LPBF}$ evaluated according to Lorusso *et al.* [27]); (ii) printing under improved microstructure conditions (M series, with high volumetric energy density to decrease the porosity content [28]). For both P and M series, a roto-translating chessboard scanning strategy was adopted (area of the printing boxes: 4x4 mm^2 for P

samples and 3x3 mm^2 for M samples) with skywriting mode enabled. Every next layer the scanning pattern was rotated by a 45° angle. For each processed layer a contouring procedure was performed.

Table 1 LPBF process parameters for the production of A357 samples.

	Power (P) [W]	**Layer thickness (t) [mm]**	**Hatch spacing (h) [mm]**	**Scanning Speed (v) [mm/s]**	**Energy density (E=P/(v*t*h)) [J/mm^3]**	**Productivity (Prod$_{LPBF}$=v*h*t) [mm^3/s]**
P	175	0.02	0.12	1400	52.08	3.4
M			0.08	500	218.75	0.8

The chemical composition of LPBF samples was checked by Glow Discharge Optical Emission Spectroscopy (GD-OES, Spectruma Analitik GDA 650) with a Grimm-style glow discharge lamp in DC mode. The analysed area was about 5 mm^2, corresponding to the internal area of the tubular anode (2.5 mm diameter). As reported in Table 2, GD-OES showed that LPBF samples retained the powder composition. In the same table, chemical composition of A357 cast samples subjected to HIP and conventional T6 used as benchmark (henceforward "C") is also reported for comparison. Chemical composition of all samples showed a total correspondence to the ASTM E179-14 standard [29].

Table 2 Chemical composition (wt.%, GDOES) of LPBF investigated samples (M and P) compared with nominal composition of feedstock powders and A357 casting (C) alloy [29]. M: improved microstructure; P: maximum productivity; C: cast + T6 + HIP.

	Chemical composition (wt %)							
	Al	**Si**	**Mg**	**Fe**	**Ti**	**Zn**	**Mn**	**Others**
Powder	Bal.	6.90	0.55	0.10	0.09	<0.01	<0.01	<0.15
C	Bal.	6.88	0.59	0.073	0.16	0.09	0.01	<0.04
P	Bal.	7.02	0.54	0.09	0.15	0.08	<0.01	<0.03
M	Bal.	6.98	0.57	0.09	0.15	0.08	<0.01	<0.03
Nominal	Bal.	6.50-7.50	0.45-0.70	0.12	0.04-0.20	0.05	0.05	*max* 0.10

A novel T6 rapid heat treatment (T6R) tailored on the peculiar LPBF microstructure, designed and optimised in a previous work [18], was carried out on M samples (henceforward "M-T6R"), so as to investigate the effect of T6R on tribological behaviour at the highest applied load used in this work (i.e., 60 N). T6R involved a short-time solution treatment (ST) at 540 °C for 10 minutes, followed by room temperature water quenching (WQ) and artificial aging (AA) at a temperature of 150 °C for 4 hours.

2.2 Microstructural, topographic, and micro-mechanical characterization

Porosity measurements were performed on optical micrographs using the ImageJ software for image analysis to estimate the density of the produced samples.

The microstructural characterization of samples was performed on metallographic sections prepared following standard polishing techniques and chemically etched with Weck's reagent (3g NH_4HF_2, 4 ml HCl, 100 ml H_2O) and Keller's reagent (1 mL HF, 1.5 mL HCl, 2.5 mL HNO_3, 95 mL H_2O). The cross-sectional microstructural observations were performed by optical (Zeiss Axio Imager A1) and scanning electron (FEG-SEM Tescan MIRA 3) microscopy, considering the directions parallel (XZ and YZ) and perpendicular (XY) to the building direction (BD) i.e., the Z axis (Fig. 1). Free surfaces were analysed before dry sliding by scanning electron microscopy as well as by stylus profilometry

(Hommelwerke T2000, tip radius: 5 μm) to evaluate roughness parameters along the direction perpendicular to the wear tracks, using Lt=12.5 mm (i.e. evaluation length), Lc=2.5 mm (i.e. sampling length) according to ISO 4288-1998 [30]. The surface topography was also investigated by eucentric tilting of the specimens during FEG-SEM observations on areas of about 0.01 mm² with Alicona MeX 6.2.1 imaging software.
Hardness measurements were carried out both on the macro- and the micro-scale by Brinell HBS 2.5/62.5/15 hardness tests (i.e., HB10, as reported in ASTM E10-18 standard) and Vickers $HV_{0.1}$ micro-hardness tests (Isoscan Galileo micro-hardness tester) in random areas of polished cross sections, respectively.

2.3 Dry sliding tests

Dry sliding tests were performed with a block-on-ring contact geometry (ASTM-G77 [31]). In this configuration, A357 stationary bars (5x5x70 mm^3) are in contact with a rotating cylinder (AISI 52100 i.e., 100Cr6 bearing steel, diameter: 40 mm, Ra: 0.09 ± 0.03 μm, 62 HRC).

Even though tribological studies on LPBF-AlSi10Mg and AlSi12 alloys were occasionally conducted against ceramic countermaterials such as Si_3N_4 [15] and Al_2O_3 [10], most of the literature studies reported to use steel as the counterpart [7–9,11,12,16,17,20,32]. Moreover, the majority of industrial applications of AlSi alloys, where components lightweighting and engine downsizing are promoted by the complex geometries enabled by LPBF, are often related to sliding wear processes against steel [33]. Based on the above, 100Cr6 bearing steel (equivalent to AISI 52100) was selected as the counterpart.

Each test was performed in ambient conditions (T≈20 °C and relative humidity 50-60%), at a constant sliding speed (0.3 ms^{-1}) and using normal loads of 20, 40 and 60 N. The selected normal loads resulted in maximum Hertzian contact pressures of 61, 86 and 105 MPa, respectively. Friction force values were continuously measured during each test as a function of the sliding distance, using a bending load cell. At least two repetitions were carried out for each testing condition. The Coefficient of Friction (COF) was firstly averaged over the steady-state regime (200-1000 m) for each test, then averaged again over the repetitions of each test.

The maximum wear depth (WD) on the sliders and on the cylinder was determined at the end of each test by means of stylus profilometry, measuring at least three profiles on each wear scar (one in the centre and two at the sides). The worn surfaces were characterized using a Zeiss EVO 50 scanning electron microscope, equipped with an energy dispersion microprobe (EDS Oxford Instruments acts-x), to identify the dominant wear mechanisms. Moreover, the cross-sectional morphology of wear tracks at load conditions of 60 N, prepared using metallographic techniques described in section 2.2, was analysed, and compared by means of optical microscopy and FEG-SEM microscopy. Finally, Vickers $HV_{0.1}$ micro-hardness measurements were carried out in cross section at 20-30 μm depth below wear tracks.
Two-way ANOVA tests with replication were adopted to assess if a statistically significant difference in the effect of load and type of samples (C, P, M) on COF and WD had to be considered.

LPBF A357 bars were tested in the as-built condition. The influence of T6R was investigated only for M samples at the highest load (60 N). The investigated A357 samples are summarised in Tab. 3.

Table 3 Summary of A357 samples.

Slider	Manufacturing	Surface finishing	Heat treatment (HT)
C	Sand cast	Mechanical machining	HIP + conventional T6
P	LPBF	As-built	-
M	LPBF	As-built	-
M-T6R	LPBF	As-built	T6R

3. Results and discussion

3.1 Microstructural and micromechanical characterization

Figure 1 shows isometric representations of the microstructure after chemical etching, both for sand-cast A357 and for as-built LPBF M and P samples. For each sample, the isometric representations show the cross sections along the following planes: (i) XY, perpendicular to the building direction (BD) (i.e., Z axis); (ii) XZ, parallel to BD and corresponding to the surfaces used for tribological tests (grey surface in the scheme of Fig. 1); (iii) YZ.

Firstly, it is worth noting the influence of the manufacturing process on microstructure: the cast samples showed, under light microscopy, the typical solidification microstructure of AlSiMg alloys (Figs. 1a,b), characterized by α-Al dendrites (secondary dendrite arm spacing, SDAS = 51.8 ± 2.7 µm) surrounded by modified eutectic with rounded Si particles (average size ranging from 5 to 10 µm). The microstructure of cast samples was homogeneous among all the analysed sections (Fig. 1a). Conversely, LPBF samples (Figs. 1c-f) did not show an isotropic microstructure. Typically, in the XY cross sections, as-built LPBF samples showed overlapping ellipsoidal scan tracks, while in the longitudinal XZ sections they showed semi-cylindrical melt pools.

Comparing XZ longitudinal section of LPBF samples (Figs. 1d,f), the different process conditions resulted in shallower and more elongated melt pools in M than P, suggesting that they were significantly affected by the scanning parameters, thus by the different thermal cycles induces by the laser scans. In T6R samples, any trace of laser tracks disappeared and a very fine and homogeneous microstructure, not fully appreciable at low-magnification optical microscopy, was observed (Figs. 1g,h).

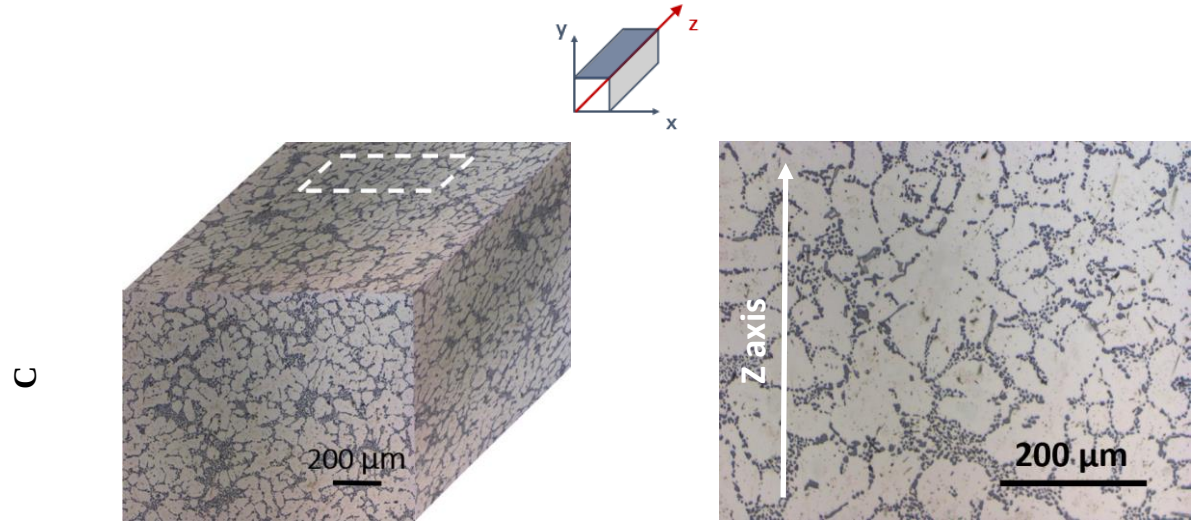

(a) (b)

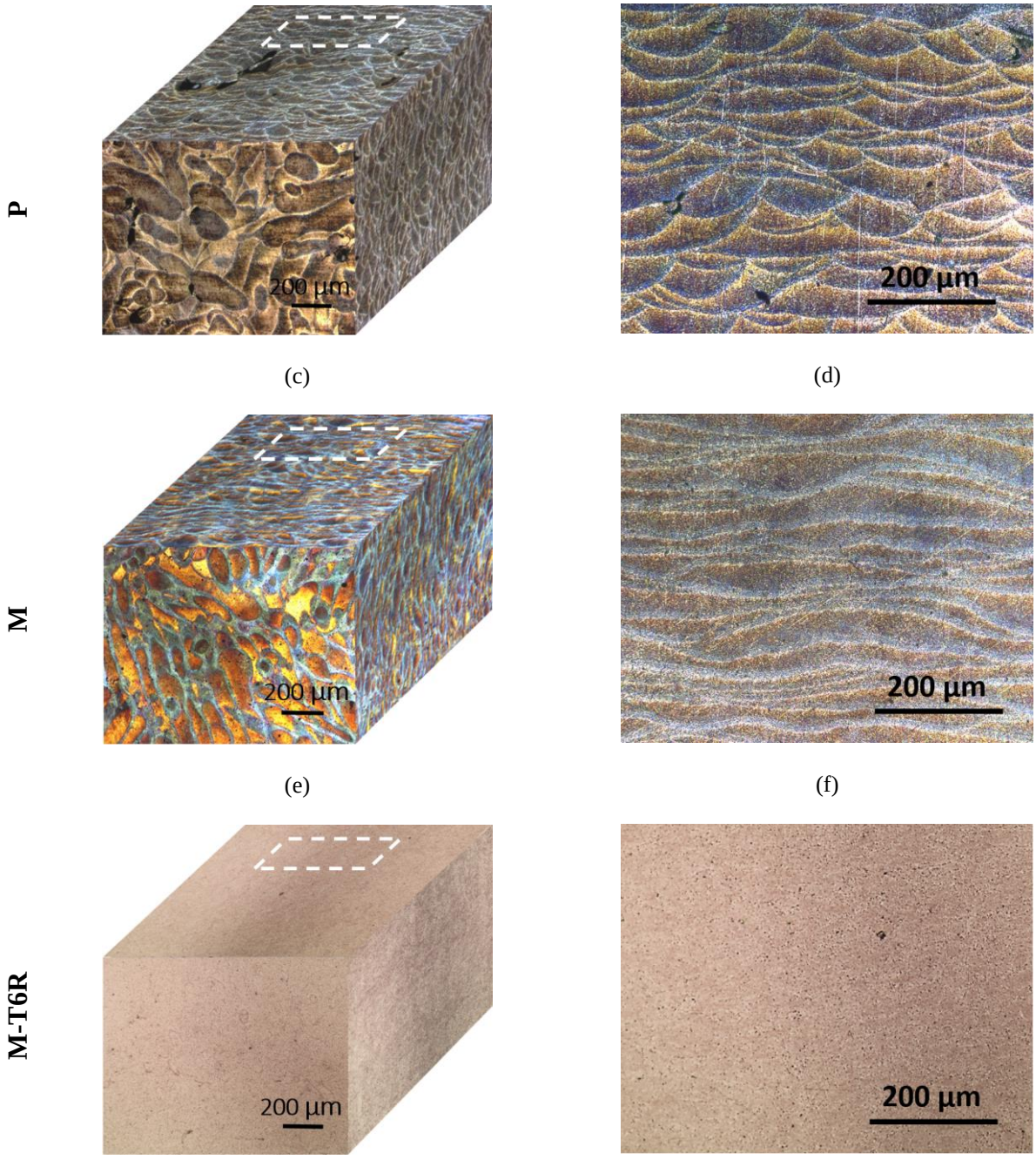

Fig. 1 Isometric representations (a,c,e,g) showing the microstructure of A357, with high magnification details of the XZ plane (b,d,f,h) used for tribological tests. Building direction: Z axis. (bright-field optical microscopy; etching: Weck's).

Considering the dark-field optical images of XY cross sections in Fig. 2 (perpendicular to the surfaces subjected to tribological tests), M showed a more homogeneous microstructure, with finer scan tracks and a lower volume fraction of porosity, than P.

The reduced porosity content was attributed to the lower scanning speed and reduced hatch spacing used for the M series, which resulted in a higher energy density (218.75 J/mm^3) compared to P (52.08 J/mm^3). Although higher productivity can be advantageous in terms of reduced time-to-market, it can favour the formation of several microstructural defects (i.e. pores and lack of fusion zones) because of the high viscosity and low wettability of the melt pool [9]. In fact, coarse porosities were observed only in P, both at the border with the contouring layer (Fig. 2a) and in the bulk (Figs. 1c,d).

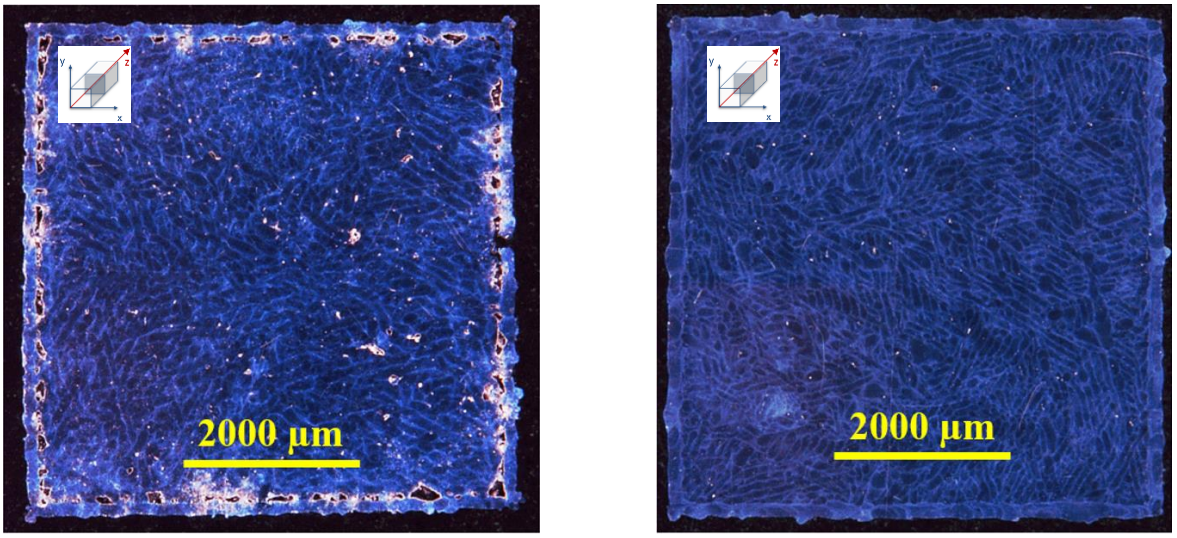

(a) (b)

Fig. 2 Low magnification dark-field images of LPBF samples (cross section along the XY plane, perpendicular to the build direction): (a) P and (b) M, showing the influence of process and contouring parameters (etching: Keller's).

At higher magnification (FEG images in Figs. 3a-d), LPBF samples showed an extremely fine microstructure within the melt pools, with sub-micrometric α-Al cells (dark zones), surrounded by an interconnected network of eutectic Si (bright zones), with an average size of about 0.1-0.2 µm. These microstructural features derived from the extremely rapid cooling and high thermal gradient induced by LPBF, which lead to the formation of a solid supersaturated and metastable solution, characterized by an extremely fine microstructure [34]. Borders of the melt pools typically showed a coarser microstructure than the core, as a result of thermal cycles induced by the processing of consequent layers inducing also a heat affected zone (HAZ) [1,14]. The contrast induced by the size variation between finer and coarser α-Al cells is responsible for highlighting the melt pools in low-magnification optical micrographs, such as those in Figures 1c-f. The microstructural anisotropy observed at low magnification persisted also at higher magnifications. In fact, in the longitudinal section (XZ, Figs. 3a,c), the α-Al cells were elongated towards the direction of the thermal gradient. Conversely, the perpendicular section (XY, Figs. 3b,d) showed fine equiaxed α-Al cells surrounded by eutectic Si.

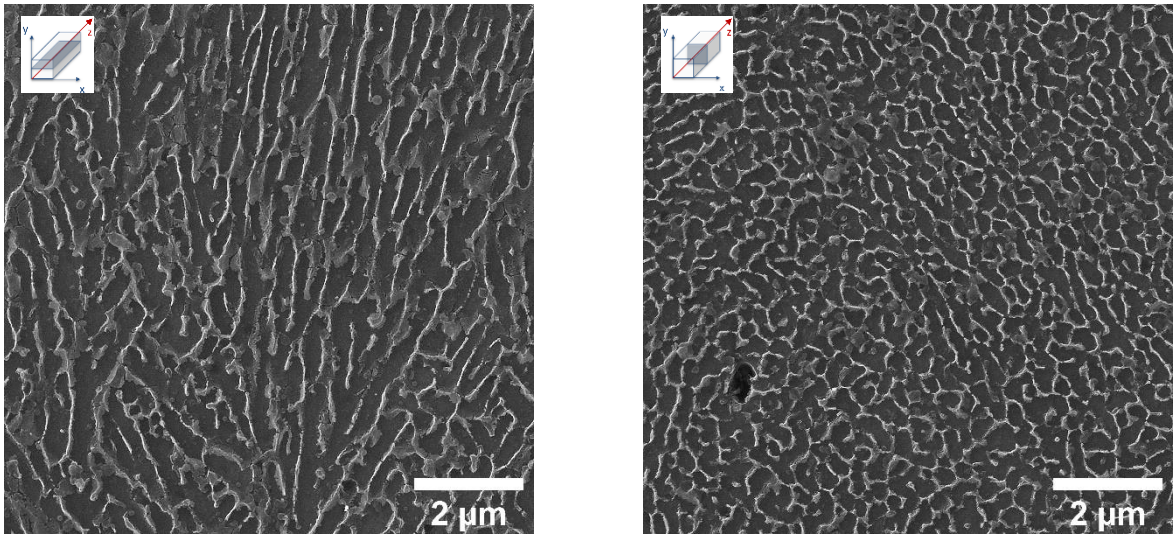

(a) (b)

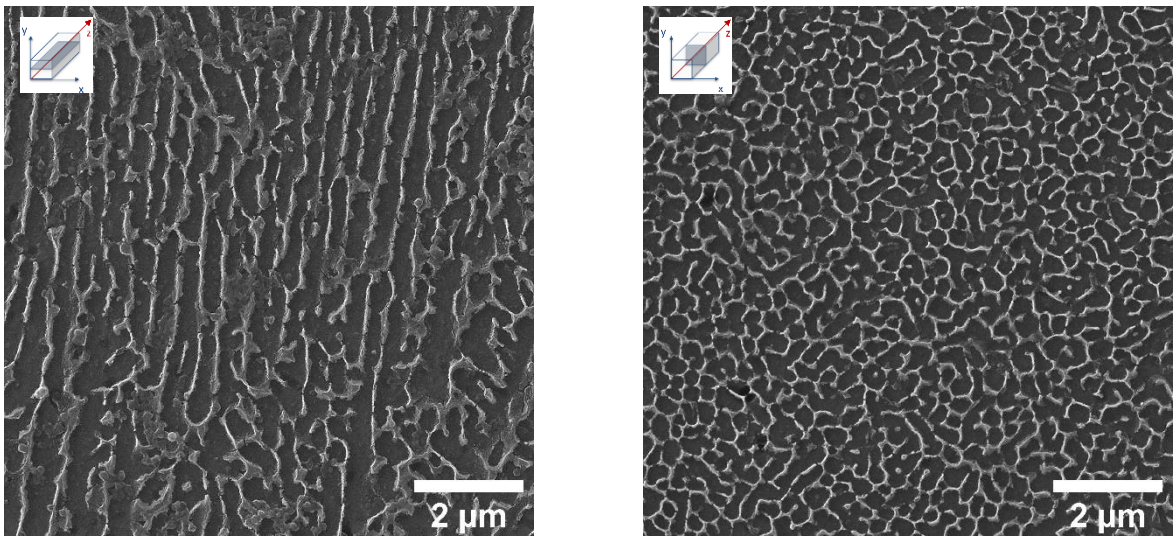

(c) (d)

Fig. 3 FEG-SEM micrographs showing the longitudinal section XZ, (a,c) and the cross section XY, (b,d) of melt pool cores in LPBF A357: (a,b) P; (c,d) M.

T6R heat treatment of M samples induced the breakdown of the fine Si-rich network that evolved into sub-micrometric globular Si particles (Figs. 4c,d), homogeneously dispersed in the Al matrix, as observed elsewhere [14,35]. Consequently, as previously mentioned, at low magnification the melt pool borders were no longer appreciable (Figs. 1g,h). Also conventional long-term T6 applied to LPBF A357 alloy leads to the formation of nearly-spherical Si particles, with size and density dependent on solution treatment temperature and time [7,14,35]. However, the shortened high-temperature exposure (i.e. 10 minutes at 540°C) of T6R induced the precipitation of Si particles with a smaller size and a rather more homogeneous distribution, also compared to conventional cast A357 T6 (Figs. 1 b,h and Fig. 4) [18].

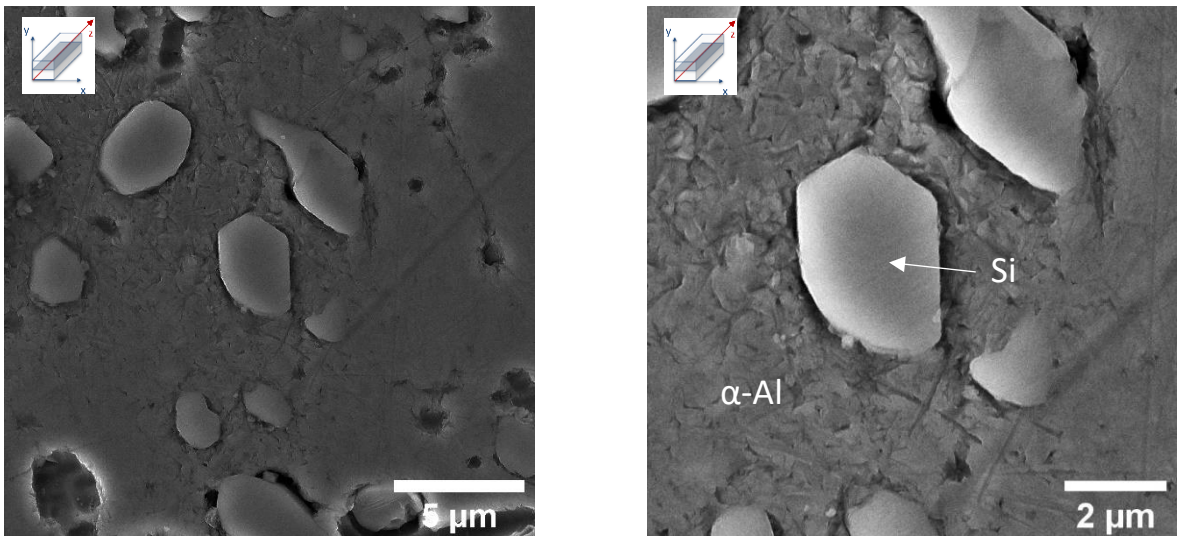

(a) (b)

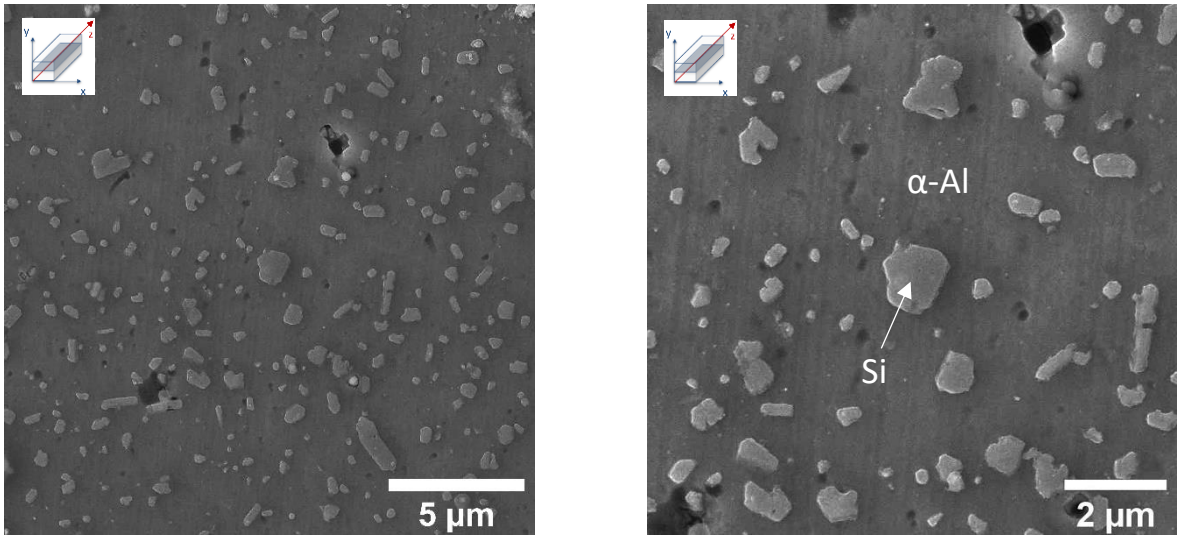

(c) (d)

Fig. 4 FEG-SEM micrographs (longitudinal section, XZ; general view (a,c) and high magnification detail (b,d)) of heat-treated A357: (a,b) C-T6; (c,d) M-T6R.

Table 4 reports the quantification of the main features of the A357 samples: relative density, hardness (measured both on the macro- and the micro-scale) as well as surface roughness (discussed in the next section).

The low density of LPBF-fabricated P samples is clearly due to the previously discussed porosity as well as to the presence of sub-surface defects, whilst M samples attained higher density values due to their improved microstructure.

Brinell hardness measurements showed that as-built LPBF samples were only slightly less hard than the sand-cast alloy (C). The higher hardness of C was clearly due to precipitation hardening induced by T6, combined with a reduced porosity content provided by Hot Isostatic Pressing (HIP). Nevertheless, the relatively high hardness of the as-built LPBF samples derived from the combined effect of other strengthening mechanisms, such as: solid solution, grain boundary, two-phases aggregates, and dispersion strengthening. After T6R, HB10 values slightly decreased (6-8% for M-T6R) in comparison to the as-built condition. Such hardness decrease is presumably related to microstructure coarsening, disruption of the eutectic Si network and precipitation of Si particles from the supersaturated α-Al matrix, inducing also a substantial stress relieving [14,18,21]. Therefore, the morphology of the Si-rich second phase (either in the form of a continuous network in the as-built condition or as coarsened, discrete particles after T6R), is likely to be primarily responsible for the observed hardness variations.

Microhardness measurements confirmed the trends observed on the macroscale, highlighting also that M samples showed the lowest $HV_{0.1}$ standard deviation value in the XZ plane (corresponding to the surface used for the tribological tests). The lower dispersion of data was associated to a considerably finer and more homogeneous microstructure in terms of size and distribution of the eutectic Si, as also observed by other Authors [11]. In our work, the improved-microstructure scanning strategy was probably responsible for this phenomenon, even if the best results in terms of lower $HV_{0.1}$ standard deviation were obtained by the M-T6R samples, probably because of the stress relieving effect during T6R itself.

Table 4: Surface roughness, hardness (HB10 and $HV_{0.1}$), and relative density of A357 bars used for tribological tests (XZ surface).

Sample	**Surface roughness (µm)**						**HB10**		**$HV_{0.1}$**	**Density (%)**
	Stylus profilometry		*Eucentric tilting*							
A357	**R_a**	**R_q**	**S_a**	**S_q**	**S_{Sk}**	**S_{Ku}**	**XY**	**XZ**	**XZ**	-
C	0.43 ± 0.05	0.63 ± 0.05	0.18 ± 0.03	0.25 ± 0.05	-0.55 ± 0.10	10.3 ± 4.8	116 ± 2	116 ± 2	129 ± 7	100.0 ± 0.04
P	9.3 ± 1.3	12.5 ± 2.3	13.1 ± 6.1	16.4 ± 6.8	0.40 ± 0.15	2.2 ± 1.2	113 ± 4	111 ± 1	122 ± 7	98.5 ± 1.1
M	15.9 ± 3.8	22.9 ± 6.2	21.9 ± 7.9	20.9 ± 9.2	0.48 ± 0.16	2.7 ± 0.9	112 ± 1	112 ± 2	116 ± 3	99.9 ± 0.03
M-T6R	-	-	-	-	-	-	106 ± 4	102 ± 2	103 ± 2	99.9 ± 0.03

3.2 Surface roughness and morphology

As far as the surface quality of the investigated samples is concerned, R_a and R_q data measured by stylus profilometry (Table 4) emphasized the high roughness typically induced by LPBF and related to the process parameters. The lower surface roughness of C samples derived from machining, carried out to obtain bars from an engine block (as shown by the grooves in SEM micrographs of Fig. 5a). Considering LPBF samples, the high roughness detected on M was likely caused by the higher energy density which promoted the attachment of particles on surface and lead to a roughness increase. Also other Authors reported that increasing energy density values can lead to vaporization of Al and Mg, thus causing development of irregular borders and introducing discrepancy in part dimensions accuracy [9].

The topography of the surfaces subjected to dry sliding tests was investigated also by eucentric tilting of the specimens during FEG-SEM observation (images in Fig. 5 and quantitative parameters in Tab. 4), in order to measure S_a (average height), S_q (root-mean-square height) as well as parameters describing the shape of the surface height probability density distribution (i.e., skewness S_{Sk} and kurtosis S_{Ku}), which may affect the tribological behaviour. In particular, skewness and kurtosis describe the shape of the probability distribution of heights and, in particular, S_{Sk} represents the asymmetry of the distribution, whilst S_{Ku} measures the flattening, or sharpness, of the distribution [36,37]. In agreement with stylus profilometry, LPBF surfaces showed the highest S_a and S_q values. The machining procedure of cast samples produced grooved surfaces with $S_{Sk}<0$ (i.e., valleys prevailing over peaks) and high S_{Ku}, hence with a distribution close to the mean value [38]. On the other hand, LPBF surfaces revealed $S_{Sk}>0$, thus with asperities prevailing over valleys, with low S_{Ku} indicating a flat distribution more dispersed along the mean value than C.

Roughness values derived by both methods (stylus profilometry and eucentric tilting) are basically consistent: slight differences between measurements can be ascribed to the different size of the analysed area (evaluation area of about 0.1 mm x 0.1 mm for eucentric tilting vs. evaluation length Lt of 12.5 mm for stylus profilometry).

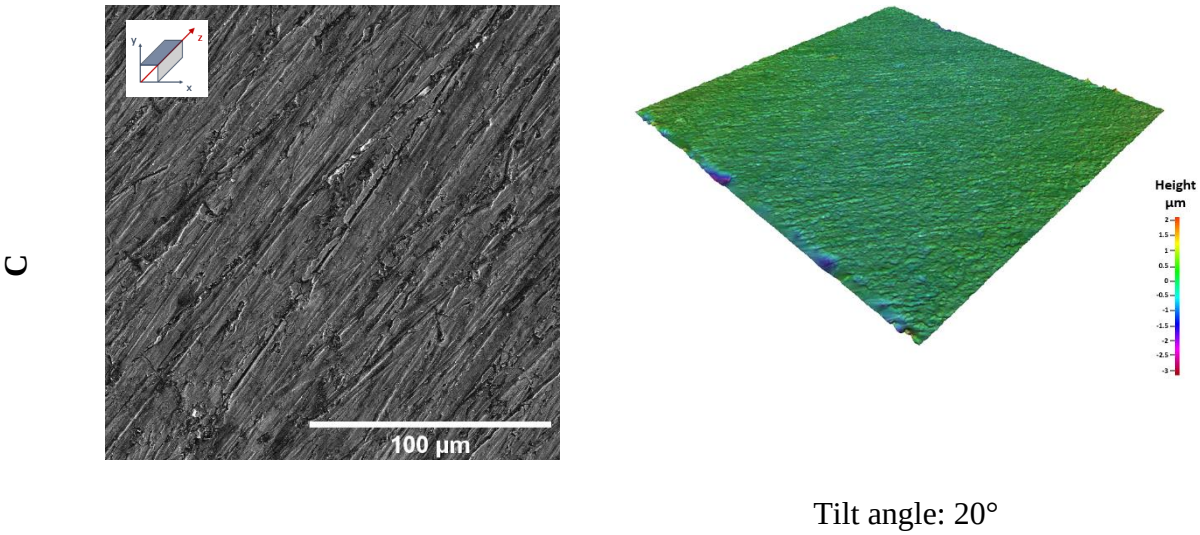

(a)

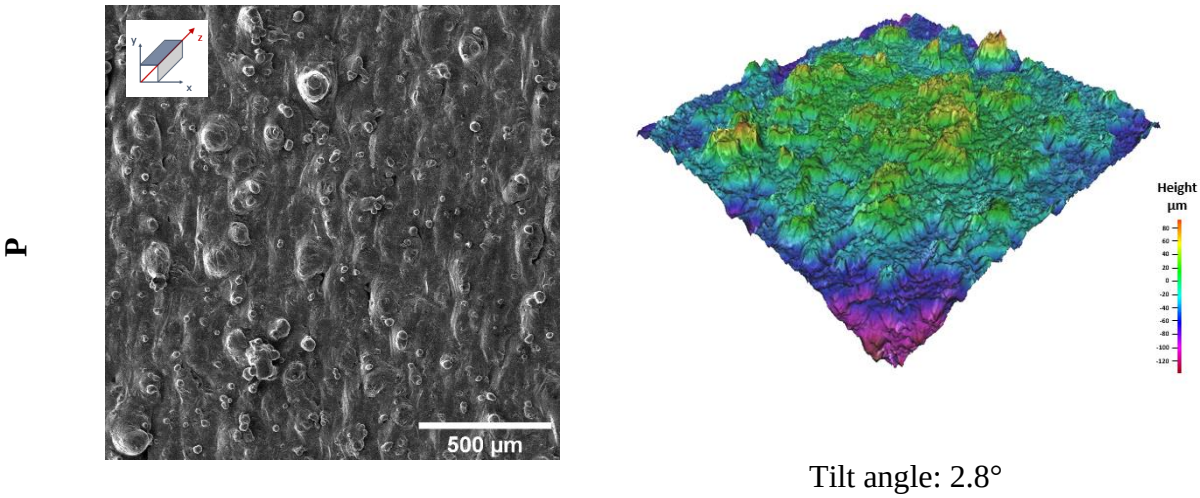

(b)

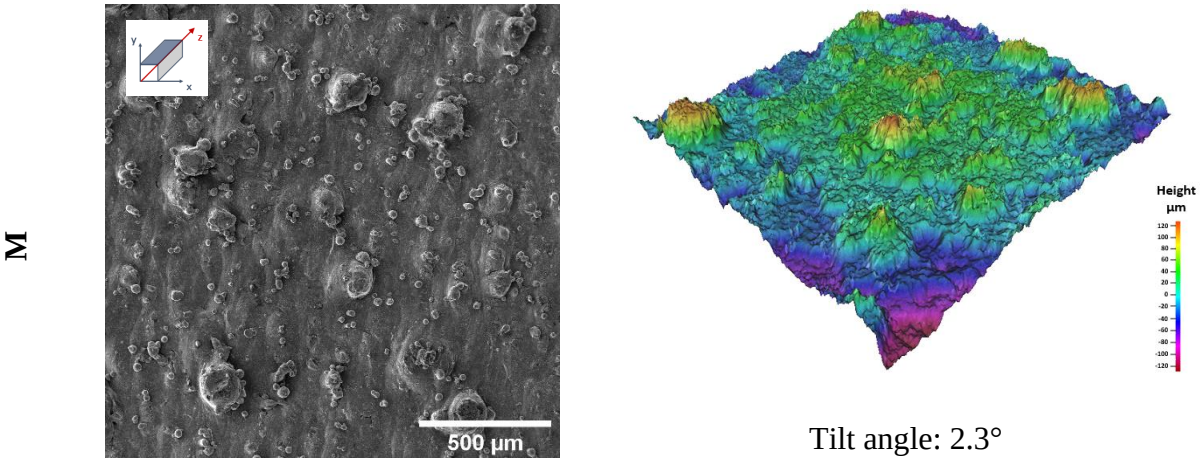

(c)

Fig. 5 Free surface topography of the A357 alloys (XZ plane): (a) C; (b) LPBF-P and (c) LPBF-M. Secondary electron (SE) images on the left and surface topographies obtained by eucentric tilting on the right.

3.3 Dry sliding tests

Figure 6 compares the coefficient of friction (COF) against AISI 52100 steel of the C, P, M and M-T6R samples as a function of sliding distance at the highest load (60 N): for all samples, COF values reached the steady-state regime after about 50 m. Then, all the samples showed a similar COF evolution, characterized by extensive fluctuations because of stick-slip which typically occurs in aluminium-steel dry sliding contact at low sliding speed, due to high adhesion work [39].

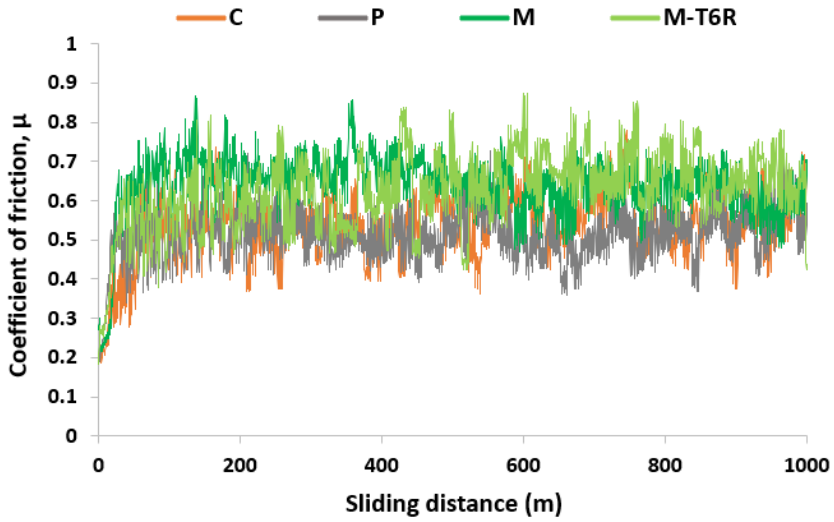

Fig. 6 Coefficient of friction (COF) as a function of sliding distance for the A357 samples, dry sliding against AISI 52100 steel (load: 60 N, speed: 0.3 m s^{-1}).

A comparison between the average steady-state values of COF and the maximum wear depths (WD) of C, P and M samples, as a function of normal load, is shown in Figures 7a,b. It is worth noting that WD on the steel counterpart were always non-detectable regardless of the normal load.

Firstly, in terms of frictional behaviour, all the samples showed COF values between 0.5 and 0.7 (typical of the aluminium-steel contact [40]) in all the investigated conditions. The cast alloy apparently showed slightly lower COF values that LPBF samples, which can be associated with low S_{Sk} and high S_{Ku} values [36,41] (Tab. 4). However, ANOVA tests showed that COF is not significantly affected both by normal load and by processing conditions (C, P or M series). The formation and stabilization of an oxide-based transfer layer (discussed below), which levelled out the protruding asperities in LPBF samples and filled up the grooves on the cast alloy surface, contributed to homogenize the frictional behaviour of all samples.

As regards wear behaviour, ANOVA tests showed that WD is affected in a statistically significant way both by load and by sample type. As-built LPBF samples interestingly showed similar WD compared to C, due to the very slight difference of hardness. Moreover, M samples also showed lower WD compared to C (Fig. 7b), due to their fine and dense microstructure.
Even though C was characterized by slightly higher Brinell and micro-Vickers hardness (due to the application of HIP and T6), its lower wear resistance compared to M (tested without any post-process treatment) can be related to its coarser and less homogeneous microstructure. HIP almost completely removes pores and shrinkage cavities formed during casting, but the coarser microstructure of cast alloy, with larger and less dispersed Si particles (as discussed in section 3.1) was considered the main reason for this behaviour.

On the other hand, P highlighted the highest WD, even when compared to C. The low wear resistance of P is probably related to the higher volume fraction of pores and the presence of sub-surface defects (Fig. 2), that led to a lower density (Table 4). In fact, according to Zhu *et al.* [6], a low densification of the material due to the presence of defects, that locally act as stress intensifiers, can result in an

higher probability of nucleation and propagation of cracks under severe dry sliding conditions [42]. The detrimental effect of sub-surface pores on the wear resistance of AlSi10Mg alloy was also confirmed by finite element simulations conducted by Talemi [43].

Figs. 7c,d includes friction and wear results of M-T6R in the comparison, so as to highlight the influence of heat treatment on the tribological behaviour of LPBF samples, assessed at the highest load (at 60 N). The rapid-solution T6R treatment slightly improved the tribological behaviour (both in terms of COF and WD) in comparison to as-built M, even though it led to slightly lower hardness values (Tab. 4). As mentioned in the Introduction, conflicting results can be found in literature regarding the tribological behaviour of LPBF samples before and after conventional T6 [16,17,20], most likely due to differences in the T6 parameters as well as in tribological testing conditions.

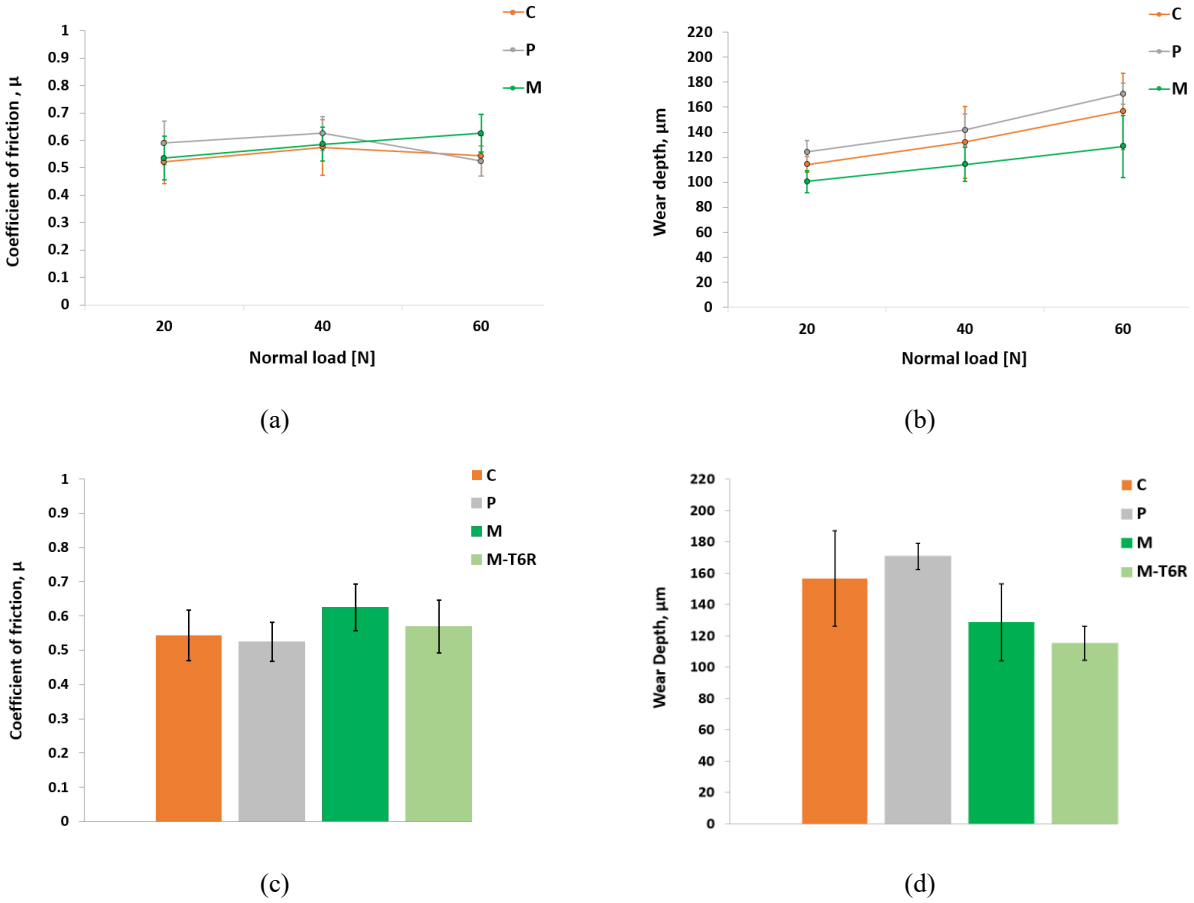

Fig. 7 Coefficient of friction COF (a) and maximum wear depths (WD) of the tracks (b) on A357 sliders as a function of applied load. COF (c) and WD (d) comparison at 60 N including M-T6R.

To better understand the tribological behaviour, the morphology and composition of the wear tracks (Figs. 8, S1) were investigated. The formation of a transfer layer was observed for all the tested conditions.

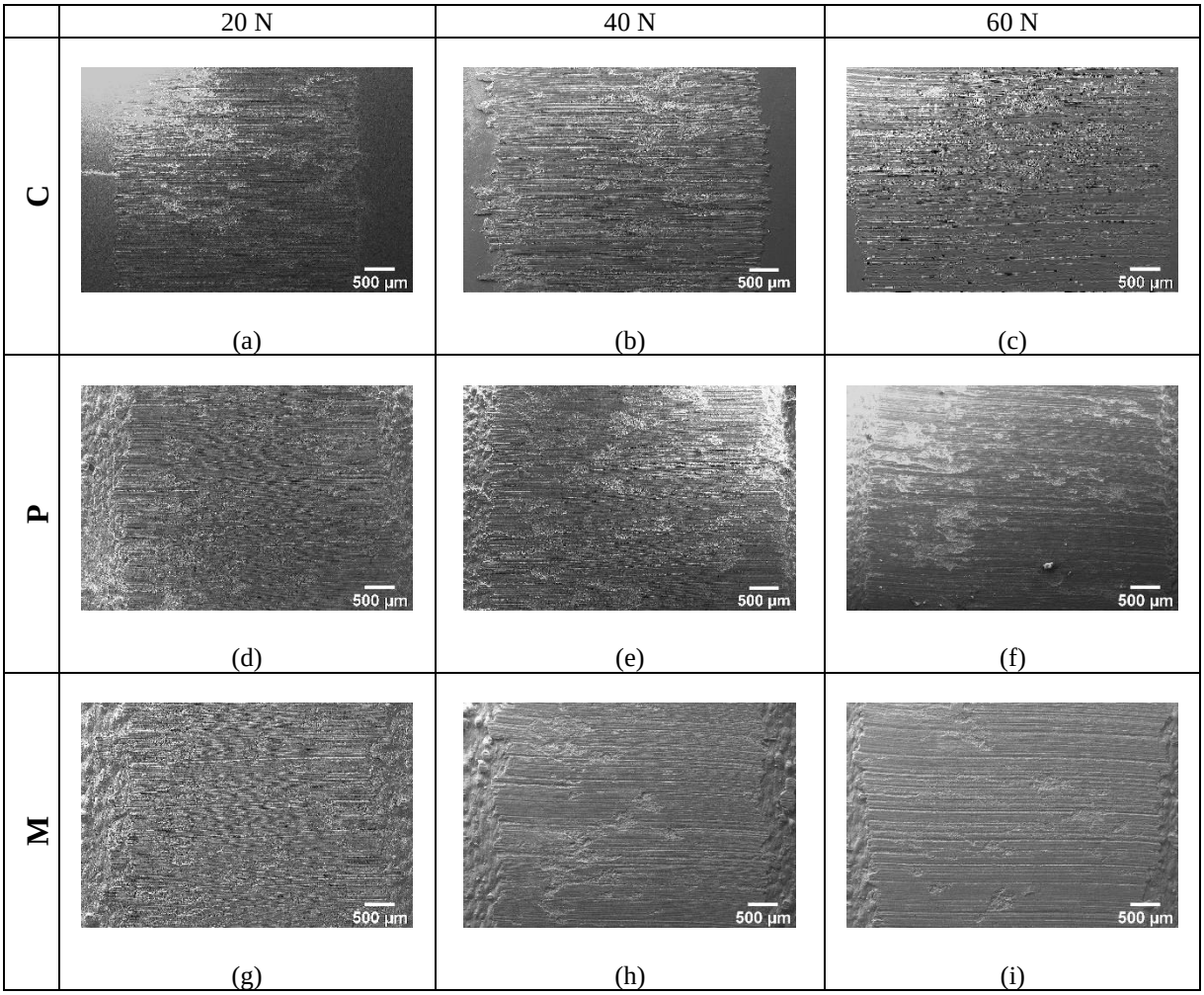

Fig. 8 SEM micrographs of the wear tracks on the surface of stationary A357 after dry sliding against AISI 52100 steel.

Localised EDS analyses showed that the transfer layer consisted mainly of mixed Al and Fe oxides (Fig. S1). A higher concentration of Fe oxides was detected within the areas where the layer was most subjected to delamination, likely due to the achievement of a critical thickness [44]. The development of such a mixed oxide transfer layer (or mechanically-mixed layer [45]) was frequently observed also by other Authors in dry sliding tests against steel [11,46]. Therefore, only mild tribo-oxidation was observed in all the investigated conditions, whilst severe wear due to delamination was never detected.

Cross sections of the wear tracks produced at the highest load (60 N) are shown in Figure 9. Micro-fragmentation associated with the presence of clusters of coarse Si particles was observed in the cast alloy (C) (Fig. 9a), whilst the wear track cross section of LPBF M samples showed higher homogeneity and no microcracks, due to the finer microstructure. Comparing M and P (Figs. 9b,c), the previously-discussed defects at the bulk-contour interface of P led to micro-fragmentation phenomena caused by the nucleation and propagation of cracks, as observed also by other Authors [20,46]. It is worth noting that this phenomenon was not observed in the case of M. When analyzing the influence of T6R on M (Fig. 9d), the Si refinement induced by the optimised heat treatment (in comparison to conventional T6 in the cast alloy) showed a beneficial effect on the tribological behaviour. This was probably related to the decrease of stress concentration at the particle/matrix interface, thereby increasing the ability to transfer load from the soft Al matrix to the harder Si particles and preventing decohesion or particle cracking [17,33]. In fact, small-sized and well-dispersed Si particles generally improve the wear resistance of the alloy, being less prone to

detachment and leading to a reduction of the abrasive component of friction and wear. Moreover, small-sized particles are less prone to induce the formation of cracks, which may cause subsurface delamination [33]. Hence, M-T6R samples show a slightly improved tribological behaviour in comparison to C, M and P.

It is also worth noting that $HV_{0.1}$ micro-hardness measured at a constant distance from the bottom of wear track showed a hardness increase of 27 % for P and 33% for M, attributable to the concurrent effect of both strain hardening by plastic deformation and precipitation hardening induced by the temperatures achieved at the contact interface, with the latter being probably the dominant strengthening process. This was confirmed by FEG-SEM observation of the areas below the contact interface (Fig. 10), where size and morphology of the Si-rich phase changed in comparison to the bulk, due to increased temperatures achieved during dry sliding.

On the other hand, C showed a slight hardness decrease (-8.50 %), likely due to mild over-aging induced by frictional heating [47]. Conversely, M-T6R showed a micro-hardness increase of 9.20 %: since T6R allowed to achieve the peak-hardening condition [18], this finding might be attributed solely to strain hardening during sliding.

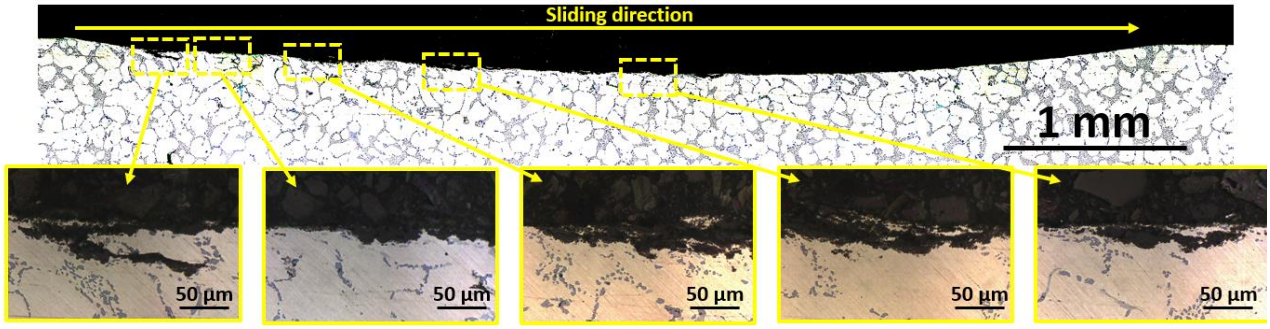

(a)

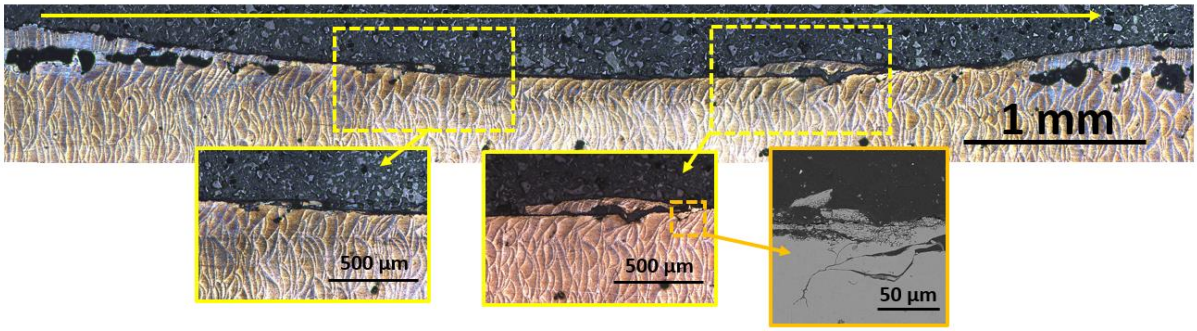

(b)

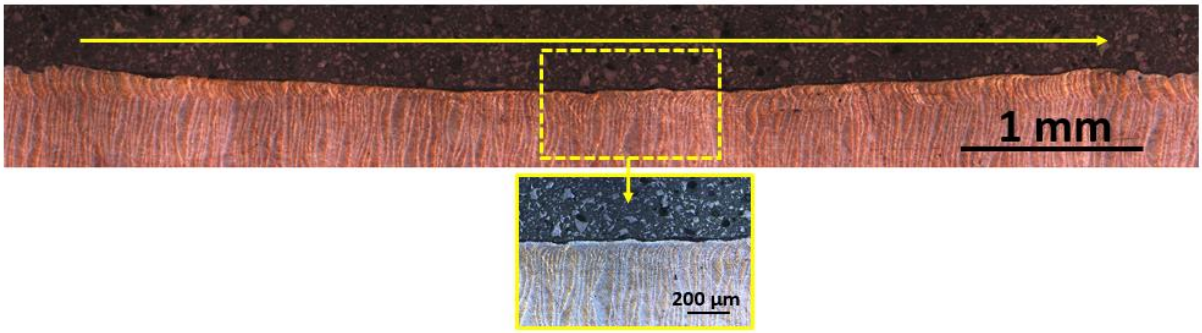

(c)

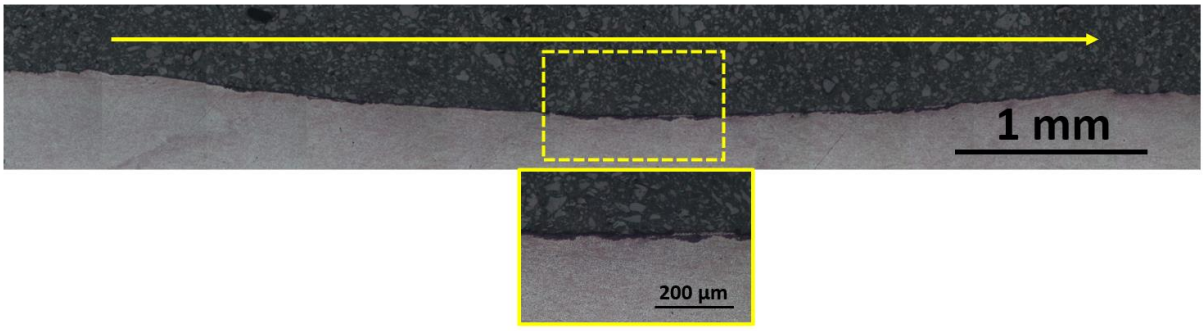

(d)

Fig. 9 Cross-section micrographs of the wear tracks on A357: (a) C; (b) P; (c) M; (d) M-T6R.

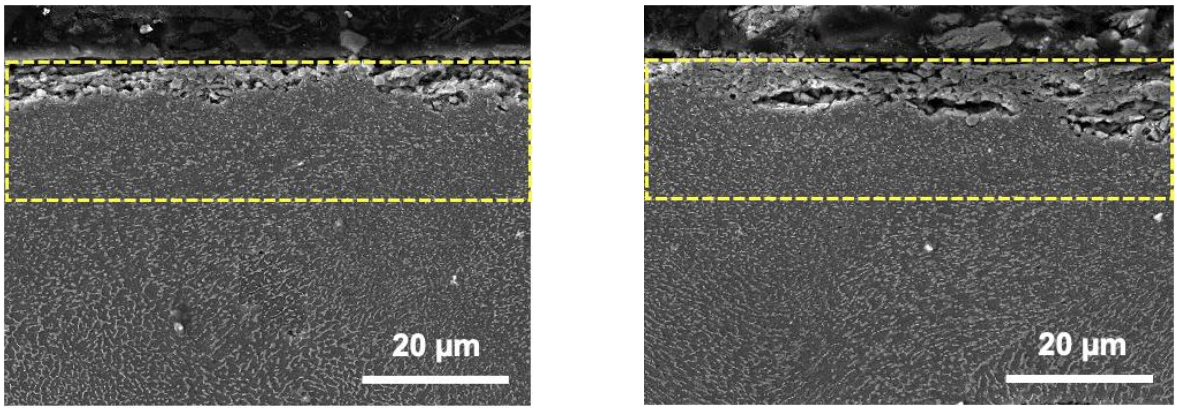

(a) (b)

Fig. 10 Cross-section FEG-SEM images of the wear tracks on as-built LPBF A357: (a) M; (b) P. The yellow dashed line highlights the area below the contact interface where size and morphology of the Si-rich phase changed as a consequence of dry sliding.

Localised SEM/EDS analysis were performed in cross-section underneath the wear track, in order to clarify the role of Si particles in the wear mechanism. The cast alloy C (Fig. 11a) showed the presence of coarse Si particles in the mechanically-mixed layer, confirming the debonding and pull-out of Si particles from the α-Al matrix, which typically occurs during dry sliding of cast Al-Si alloys against steel [33,42]. When this phenomenon occurs, Si particles can act as an abrasive third body, sharply increasing wear loss [33]. On the other hand, sub-micrometric sized Si particles of M-T6R were embedded into the deepest zone of the transfer layer, contributing to stabilize it, and leading to increase its load-bearing capacity (Fig. 11b). As also observed elsewhere [7], the smaller the size of Si particles the lower the wear rate.

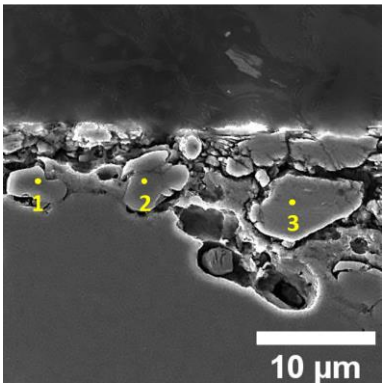

%w/w	O	Al	Si	Fe
1	0.53	1.18	**97.73**	0.56
2	0.27	0.42	**99.31**	-
3	33.83	33.64	1.81	30.72

(a)

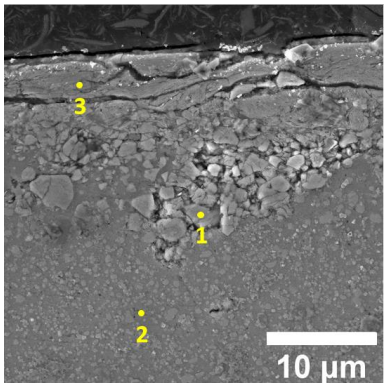

%w/w	O	Al	Si	Fe
1	35.71	31.89	**8.57**	23.83
2	1.06	97.04	1.17	0.73
3	35.91	38.56	**5.86**	19.67

(b)

Fig. 11 SEM/EDS analyses of the cross sections underneath wear tracks on heat-treated A357, showing Si particles embedded in the transfer layer: (a) cast alloy (C-T6); (b) LPBF M-T6R.

4 Conclusions

The influence of two combinations of process parameters (maximum productivity, P and improved microstructure, M) on the microstructure and the tribological behaviour of the A357 Al-Si-Mg alloy fabricated by LPBF, dry sliding against quenched and tempered AISI 52100 steel, was evaluated. The same alloy produced by sand casting, and subsequently subjected to Hot Isostatic Pressing (HIP) and T6 heat treatment (C), was used as a benchmark. Moreover, a novel T6 heat treatment procedure with rapid solution treatment (T6R) was applied to M samples (providing the higher wear resistance in the as-built condition), to investigate the effect of heat treatment on tribological behaviour at the highest applied load.

The following conclusions can be drawn from this work:

- The LPBF as-built samples showed a much finer and more homogeneous microstructure than the cast A357 alloy: this allowed as-built LPBF samples to attain hardness values comparable to those of the cast and T6-treated alloy. LPBF process parameters selected for M allowed to improve the microstructure in terms of reducing porosities and increasing microstructural homogeneity, in turn improving the uniformity of the micro-hardness. After T6R, the LPBF microstructure evolved into a fine distribution of sub-micrometric globular Si particles, with a more homogeneous distribution compared to conventional T6 applied to the cast alloy.
- All the A357 samples provided similar COF values, regardless of the manufacturing route, surface roughness and applied load. M showed a higher wear resistance than C (due to the finer microstructure) and P (due to the lower sub-surface porosity). After T6R, M showed a slight improvement of the friction and wear behaviour than in the as-built condition.
- Mild tribo-oxidative wear, with the formation of a compact oxide transfer layer, was always observed. While the coarse Si particles of C showed a high tendency for detachment from α-Al matrix, P was more prone to micro-fragmentation and cracks nucleation underneath the wear track due to sub-surface defects; these phenomena were not observed for M. The sub-micrometric size of Si particles produced by T6R prevented debonding from the α-Al matrix and allowed embedding into the transfer layer during the contact, contributing to increase the wear resistance.
- Dry sliding probably induced both strain- and precipitation-hardening under the contact interface in LPBF samples, while the cast alloy was likely affected by mild over-aging. Since M-TR6 had already achieved the peak-hardening condition, its micro-hardness increase was attributed to strain-hardening.

In conclusion, LPBF process with optimised process parameters allowed to improve the tribological behaviour of A357 in comparison to sand casting + HIP + T6, even without any post processing treatments. The T6R heat treatment, optimized for LPBF samples induced a further improvement of the tribological behaviour.

CRediT authorship contribution statement

L. Lorenzetti: Investigation – Data curation – Writing - original draft. L. Tonelli: Methodology – Validation. – Writing - Review & Editing. L. Ceschini: Writing - Review & Editing. E. Liverani: Methodology – Writing - Review & Editing. C. Martini: Project administration – Supervision – Formal Analysis – Writing - Review & Editing.

Declaration of competing interest

The Authors declare that they have no known competing financial interests or personal relationships that could have appeared to influence the work reported in this paper.

Acknowledgments

The Authors would like to acknowledge Dr. Iuri Boromei at the University of Bologna, Italy, for his invaluable contribution to the FEG-SEM, EDS and surface topography analysis.

This work has been supported by the former Italian Ministry for the Economic Development (MISE) through the project "1.3 Materiali di frontiera per usi energetici" (CUP: I34I19005780001) within the Three-Year Plan 2019–2021 of the National Electric System Research Fund.

5 References

[1] T. DebRoy, H.L. Wei, J.S. Zuback, T. Mukherjee, J.W. Elmer, J.O. Milewski, A.M. Beese, A. Wilson-Heid, A. De, W. Zhang, Additive manufacturing of metallic components – Process, structure and properties, Prog. Mater. Sci. 92 (2018) 112–224. https://doi.org/10.1016/j.pmatsci.2017.10.001.

[2] N.T. Aboulkhair, M. Simonelli, L. Parry, I. Ashcroft, C. Tuck, R. Hague, 3D printing of Aluminium alloys: Additive Manufacturing of Aluminium alloys using selective laser melting, Prog. Mater. Sci. 106 (2019) 1–45. https://doi.org/10.1016/j.pmatsci.2019.100578.

[3] K. Anderson, J. Weritz, J.G. Kaufman, Properties and Selection of Aluminum Alloys - ASM Handbook, ASM International, Vol. 2B (2019) 548–552. https://doi.org/10.31399/asm.hb.v02b.a0006568.

[4] K. Anderson, J. Weritz, J.G. Kaufman, Properties and Selection of Aluminum Alloys - ASM Handbook, ASM International, Vol. 2B (2019) 553-555. https://doi.org/10.31399/asm.hb.v02b.a0006569.

[5] T. Yu, H. Hyer, Y. Sohn, Y. Bai, D. Wu, Structure-property relationship in high strength and lightweight AlSi10Mg microlattices fabricated by selective laser melting, Mater. Des. 182 (2019) 108062. https://doi.org/10.1016/j.matdes.2019.108062.

[6] Y. Zhu, J. Zou, H. Yang, Wear performance of metal parts fabricated by selective laser melting: a literature review, J. Zhejiang Univ. Sci. A. 19 (2018) 95–110. https://doi.org/10.1631/jzus.A1700328.

[7] K.G. Prashanth, B. Debalina, Z. Wang, P.F. Gostin, A. Gebert, M. Calin, U. Kühn, M. Kamaraj, S. Scudino, J. Eckert, Tribological and corrosion properties of Al-12Si produced by selective laser melting, J. Mater. Res. 29 (2014) 2044–2054. https://doi.org/10.1557/jmr.2014.133.

[8] P. Thasleem, B. Kuriachen, D. Kumar, A. Ahmed, M.L. Joy, Effect of heat treatment and electric discharge alloying on the tribological performance of selective laser melted AlSi10Mg, J. Tribol. 143 (2021) 1–16. https://doi.org/10.1115/1.4050897.

[9] H. Wu, Y. Ren, J. Ren, A. Cai, M. Song, Y. Liu, X. Wu, Q. Li, W. Huang, X. Wang, I. Baker, Effect of melting modes on microstructure and tribological properties of selective laser melted AlSi10Mg alloy, Virtual Phys. Prototyp. 15 (2020) 570–582. https://doi.org/10.1080/17452759.2020.1811932.

[10] N. Kang, P. Coddet, H. Liao, T. Baur, C. Coddet, Wear behavior and microstructure of hypereutectic Al-Si alloys prepared by selective laser melting, Appl. Surf. Sci. 378 (2016) 142–149. https://doi.org/10.1016/j.apsusc.2016.03.221.

[11] J. Liu, Y. Zhou, Y. Fan, X. Chen, Effect of laser hatch style on densification behavior, microstructure, and tribological performance of aluminum alloys by selective laser melting, J. Mater. Res. 33 (2018) 1713–1722. https://doi.org/10.1557/jmr.2018.166.

[12] A.K. Mishra, R.K. Upadhyay, A. Kumar, Surface Wear Anisotropy in AlSi10Mg Alloy Sample Fabricated by Selective Laser Melting: Effect of Hatch Style, Scan Rotation and Use of Fresh and Recycled Powder, J. Tribol. 143 (2021) 1–17. https://doi.org/10.1115/1.4047788.

[13] H.J. Rathod, T. Nagaraju, K.G. Prashanth, U. Ramamurty, Tribological properties of selective laser melted Al–12Si alloy, Tribol. Int. 137 (2019) 94–101. https://doi.org/10.1016/j.triboint.2019.04.038.

[14] N.T. Aboulkhair, M. Simonelli, L. Parry, I. Ashcroft, C. Tuck, R. Hague, 3D printing of Aluminium alloys: Additive Manufacturing of Aluminium alloys using selective laser melting, Prog. Mater. Sci. 106 (2019) 100578. https://doi.org/10.1016/j.pmatsci.2019.100578.

[15] P. Wei, Z. Chen, S. Zhang, X. Fang, B. Lu, L. Zhang, Z. Wei, Effect of T6 heat treatment on the surface tribological and corrosion properties of AlSi10Mg samples produced by selective laser melting, Mater. Charact.

171 (2021) 110769. https://doi.org/10.1016/j.matchar.2020.110769.
[16] P. Tonolini, L. Montesano, M. Tocci, A. Pola, M. Gelfi, Wear Behavior of AlSi10Mg Alloy Produced by Laser-Based Powder Bed Fusion and Gravity Casting, Adv. Eng. Mater. 23 (2021) 2100147. https://doi.org/10.1002/adem.202100147.
[17] T.H. Park, M.S. Baek, Y. Sohn, K.A. Lee, Effect of post-heat treatment on the wear properties of AlSi10Mg alloy manufactured by selective laser melting, Arch. Metall. Mater. 65 (2020) 1073–1080. https://doi.org/10.24425/amm.2020.133220.
[18] L. Tonelli, E. Liverani, A. Morri, L. Ceschini, Role of Direct Aging and Solution Treatment on Hardness, Microstructure and Residual Stress of the A357 (AlSi7Mg0.6) Alloy Produced by Powder Bed Fusion, Metall. Mater. Trans. B 52 (2021) 2484–2496. https://doi.org/10.1007/s11663-021-02179-6.
[19] P. Wei, Z. Chen, S. Zhang, X. Fang, B. Lu, L. Zhang, Z. Wei, Effect of T6 heat treatment on the surface tribological and corrosion properties of AlSi10Mg samples produced by selective laser melting, Mater. Charact. 171 (2021) 110769. https://doi.org/10.1016/j.matchar.2020.110769.
[20] W.H. Kan, S. Huang, Z. Man, L. Yang, A. Huang, L. Chang, Y. Nadot, J.M. Cairney, G. Proust, Effect of T6 treatment on additively-manufactured AlSi10Mg sliding against ceramic and steel, Wear 482–483 (2021) 203961. https://doi.org/10.1016/j.wear.2021.203961.
[21] G. Di Egidio, L. Ceschini, A. Morri, C. Martini, M. Merlin, A Novel T6 Rapid Heat Treatment for AlSi10Mg Alloy Produced by Laser-Based Powder Bed Fusion: Comparison with T5 and Conventional T6 Heat Treatments, Metall. Mater. Trans. B 53 (2022) 284–303. https://doi.org/10.1007/s11663-021-02365-6.
[22] J.H. Rao, Y. Zhang, K. Zhang, X. Wu, A. Huang, Selective laser melted Al-7Si-0.6Mg alloy with in-situ precipitation via platform heating for residual strain removal, Mater. Des. 182 (2019) 108005. https://doi.org/10.1016/j.matdes.2019.108005.
[23] J.T. Oliveira de Menezes, E.M. Castrodeza, R. Casati, Effect of build orientation on fracture and tensile behavior of A357 Al alloy processed by Selective Laser Melting, Mater. Sci. Eng. A. 766 (2019) 138392. https://doi.org/10.1016/j.msea.2019.138392.
[24] R. Casati, M. Vedani, Aging Response of an A357 Al Alloy Processed by Selective Laser Melting, Adv. Eng. Mater. 21 (2019) 1–7. https://doi.org/10.1002/adem.201800406.
[25] K. V. Yang, P. Rometsch, C.H.J. Davies, A. Huang, X. Wu, Effect of heat treatment on the microstructure and anisotropy in mechanical properties of A357 alloy produced by selective laser melting, Mater. Des. 154 (2018) 275–290. https://doi.org/10.1016/j.matdes.2018.05.026.
[26] H. Rao, S. Giet, K. Yang, X. Wu, C.H.J. Davies, The influence of processing parameters on aluminium alloy A357 manufactured by Selective Laser Melting, Mater. Des. 109 (2016) 334–346. https://doi.org/10.1016/j.matdes.2016.07.009.
[27] M. Lorusso, F. Trevisan, F. Calignano, M. Lombardi, D. Manfredi, A357 alloy by LPBF for industry applications, Materials (Basel) 13 (2020) 1–12. https://doi.org/10.3390/ma13071488.
[28] L. Tonelli, E. Liverani, G. Valli, A. Fortunato, L. Ceschini, Effects of powders and process parameters on density and hardness of A357 aluminum alloy fabricated by selective laser melting, Int. J. Adv. Manuf. Technol. 106 (2020) 371–383. https://doi.org/10.1007/s00170-019-04641-x.
[29] ASTM B179-18, Standard Specification for Aluminum Alloys in Ingot and Molten Forms for Castings from All Casting Processes 1 Products for Compositional Analysis E29 Practice for Using Significant Digits in Test Data to E34 Test Methods for Chemical Analysis of Aluminum, 2019. https://doi.org/10.1520/B0179-18.
[30] ISO 4288:1998. Geometrical Product Specifications (GPS) - Surface texture: Profile method - Rules and procedures for the assessment of surface texture, 1998.
[31] ASTM G-77-17, Standard Test Method for Ranking Resistance of Materials to Sliding Wear Using Block-on-ring Wear Test, 2017. https://doi.org/10.1520/ G0077-17.
[32] P. Wang, S. Yu, J. Shergill, A. Chaubey, J. Eckert, K.G. Prashanth, S. Scudino, Selective Laser Melting of Al-7Si-0.5 Mg-0.5Cu: Effect of Heat Treatment on Microstructure Evolution, Mechanical Properties and Wear Resistance, Acta Metall. Sin. Engl. 35 (2022) 389–396. https://doi.org/10.1007/s40195-021-01279-1.
[33] L. Ceschini, S. Toschi, Friction and Wear of Aluminum Alloys and Composites - ASM Handbooks, ASM International, Vol. 18 (2017) 509–532. https://doi.org/10.31399/asm.hb.v18.a0006388.
[34] X. Liu, C. Zhao, X. Zhou, Z. Shen, W. Liu, Microstructure of selective laser melted AlSi10Mg alloy, Mater. Des. 168 (2019) 107677. https://doi.org/10.1016/j.matdes.2019.107677.
[35] K.G. Prashanth, S. Scudino, H.J. Klauss, K.B. Surreddi, L. Löber, Z. Wang, A.K. Chaubey, U. Kühn, J. Eckert, Microstructure and mechanical properties of Al-12Si produced by selective laser melting: Effect of heat treatment, Mater. Sci. Eng. A 590 (2014) 153–160. https://doi.org/10.1016/j.msea.2013.10.023.
[36] B. Sagbas, Post-Processing Effects on Surface Properties of Direct Metal Laser Sintered AlSi10Mg Parts, Met. Mater. Int. 26 (2020) 143–153. https://doi.org/10.1007/s12540-019-00375-3.
[37] R. Cai, C. Zhao, X. Nie, Effect of plasma electrolytic oxidation process on surface characteristics and tribological behavior, Surf. Coatings Technol. 375 (2019) 824–832.

https://doi.org/10.1016/j.surfcoat.2019.06.104.
[38] B. Bhushan, Surface Roughness Analysis and Measurement Techniques, in: Mod. Tribol. Handbook, Two Vol. Set, CRC Press, 2000: pp. 79–150. https://doi.org/10.1201/9780849377877-10.
[39] G. Straffelini, Wear processes. In: Friction and Wear: Methodologies For Design And Control Springer Tracts in Mechanical Engineering, Springer, Cham, 2015. https://doi.org/https://doi.org/10.1007/978-3-319-05894-8.
[40] K. Holmerg, A. Matthews, Coatings Tribology: Properties, Mechanisms, Techniques and Applications in Surface Engineering, 2nd ed., Elsevier, Amsterdam, 2009. https://doi.org/https://www.elsevier.com/books/coatings-tribology/holmberg/978-0-444-52750-9.
[41] B. Podgornik, Surface Texturing - ASM Handbooks, ASM International, Vol. 18 (2017) 706–722. https://doi.org/10.31399/asm.hb.v18.a0006365.
[42] M.A. Islam, Z.N. Farhat, Effect of porosity on dry sliding wear of AlSi alloys, Tribol. Int. 44 (2011) 498–504. https://doi.org/10.1016/j.triboint.2010.12.007.
[43] R. Talemi, A numerical study on effects of randomly distributed subsurface hydrogen pores on fretting fatigue behaviour of aluminium AlSi10Mg, Tribol. Int. 142 (2020) 105997. https://doi.org/10.1016/j.triboint.2019.105997.
[44] T.F.J. Quinn, Oxidational wear modelling: I, Wear. 153 (1992) 179–200.
[45] A.M. Rajesh, K.M. Kaleemulla, D. Saleemsab, K.N. Bharath, Generation of mechanically mixed layer during wear in hybrid aluminum MMC under as-cast and age hardened conditions, SN Appl. Sci. 1 (2019) 1–10. https://doi.org/10.1007/s42452-019-0906-5.
[46] D. Gu, J. Jue, D. Dai, K. Lin, W. Chen, Effects of dry sliding conditions on wear properties of Al-matrix composites produced by selective laser melting additive manufacturing, J. Tribol. 140 (2018) 1–12. https://doi.org/10.1115/1.4037729.
[47] X.Y. Li, K.N. Tandon, Subsurface microstructures generated by dry sliding wear on as-cast and heat treated Al metal matrix composites, Wear. 203–204 (1997) 703–708.